Journal of Materials Chemistry A

ROYAL SOCIETY OF CHEMISTRY

PAPER

View Article Online
View Journal | View Issue

Cite this: J. Mater. Chem. A, 2023, 11, 15889

Hydrogen spillover effect – harnessing hydrogen evolution reaction from diverse carbon-based supports with a tungsten oxide catalyst†

R. Rajalakshmi, G. Srividhya, C. Viswanathan and N. Ponpandian *

Engineering competent electrocatalysts to accelerate the production of sustainable hydrogen fuel is an important criterion in electrochemical water splitting. The hydrogen evolution reaction (HER) as an equally crucial step in water electrolysis has been in the spotlight for more than a decade. Nevertheless, understanding the mechanistic insights between the multifunctional catalytic sites, especially in sophisticated nanohybrids are not much delved into here, an inexpensive fabrication of a '3D electrocatalyst' with the well-established WO_3 metal oxide is layered with different carbon entities, both two dimensional and bulk, to decode the mechanism of hydrogen spillover effect (HSPE) and understand their stability profile through Pourbaix profiles for heterogeneous catalysis of HER in both acidic and alkaline environments. The HER kinetics of the reduced graphene sheets with WO_3 could stand on par with the existing state-of-the-art noble electrocatalyst – Pt. Sequentially strong electrocatalytic kinetics with high durability and intrinsic activity conclusively make the freestanding 3D architecture an attractive candidate to scale up as an efficient electrocatalyst for the HER. The present work emphasizes the need to understand the mechanism for designing and developing HER electrocatalysts based on the conductive nature and electron transport pathways on different carbon supports.

Received 26th April 2023
Accepted 25th June 2023

DOI: 10.1039/d3ta02509h

rsc.li/materials-a

1. Introduction

The diminishing quantity of fossil fuels and the adverse effects of climate change due to carbon emission have stressed the global demand for green energy production, thus promoting research interest in the development of fuel cells for energy conservation. Hydrogen is deemed the fuel of the future, owing to its high energy density and abundance of hydrogen sources.[1] Considering the practical need, hydrogen production from water splitting or water electrolysis through the Hydrogen Evolution Reaction (HER) gains immense attention in research. Hydrogen production from the HER is limited by the use of costly noble metal catalysts, inadequate stability for prolonged use under extreme pH conditions, and high operational overpotential for non-noble metal catalysts.[2] The exploration of efficient and stable materials for enhanced HER catalysis and studies on expanding the catalyzing properties of the HER in a broader pH range are the focal topics in the field of water splitting.

The near-zero Gibbs free energy ($\Delta G_H \sim 0$) for hydrogen intermediate adsorption is a critical characteristic of an ideal HER catalyst. However, only noble metals like Pt possess this trait and most non-noble metal-based catalysts suffer from adverse hydrogen adsorption/desorption kinetics, which hinders the efficiency of the HER. In light of this, metals along with conductive support materials have recently emerged as promising HER catalysts that take advantage of the hydrogen spillover effect (HSPE) for enhanced H_2 evolution.[3–6] The HSPE is the mechanism of migration of hydrogen atoms from the surface of a metal-based catalyst to the surface of an adsorbent support material. The augmentation of the HER occurs in metal–support catalysts by (i) strong adsorption of a proton on the metal surface, which has $\Delta G_H < 0$; (ii) hydrogen spillover from the metal to the support; (iii) effective desorption of hydrogen from the support surface, which has $\Delta G_H > 0$. Thus, the HSPE mechanism at the metal/support interface helps non-noble metal-based catalysts to overcome their sluggish hydrogen adsorption/desorption kinetics and thus enhances their HER activity. Similarly, non-noble metal-based catalysts should have competitive stability compared to state-of-the-art noble metals for a durable HER performance. The Pourbaix plot is used to comprehend the electrochemical stability profile of a catalyst in the entire pH spectra as a function of potential. As broad pH range operation of HER catalysts is desired, the Pourbaix stability profile is helpful to assess the long-term operation of the catalyst in different aqueous media.[7]

Numerous non-noble metal-based electrocatalysts have been put forth by the electrochemical research community as capable HER catalysts for replacing ideal noble metal catalysts. Among

Department of Nanoscience and Technology, Bharathiar University, Coimbatore, India. E-mail: ponpandian@buc.edu.in; Tel: +91-422-2428-423

† Electronic supplementary information (ESI) available. See DOI: https://doi.org/10.1039/d3ta02509h

various non-noble metal-based materials, the long-established transition metal oxides (TMOs) are some of the prominent materials for the HER. The semiconducting n-type WO_3 is a prospective entrant in the class of TMO electrocatalysts, owing to its high stability, excellent redox capability, and low cost. The band gap of WO_3 also makes it suitable for the photoelectrochemical and photocatalytic HER. A recent study concluded that WO_3 nanoplatelets composited with carbon nanofibers by the electrospinning technique revealed a small Tafel slope of 89 mV dec^{-1} and a high current density of 0.239 mA cm^{-2}.[8] The shape, structure, and optical properties of WO_3 can be easily tuned according to the intended application. Our previous work reports a material engineering strategy for tuning the shape and structure of WO_3 to intrinsically boost its HER catalytic activity.[9] Enhancing oxygen vacancies in WO_3 nanosheets improves the charge transfer properties, which in turn improved the catalytic activity with a low overpotential of 260 mV at 50 mA cm^{-2} and achieved a stable operation of 105 h.[10] The structural properties of the catalyst also have an impact on the catalyzing activity. Single crystalline WO_3 anchored on a carbon support showed notable HER catalytic activity in both acidic and alkaline media, which depicts the impressive stability of WO_3 in a wide range of pH.[11] The catalytic activity of WO_3 can be improved by doping with metals and compositing with suitable support materials.[12] Carbon allotropes are a suitable class of support materials for the hydrogen spillover that benefitted the HER, due to their chemical and economic stability and desirable hydrogen absorptivity and desorptivity.[13–16] Amidst them, two-dimensional graphene, graphene oxide (GO), reduced graphene oxide (rGO), and reduced graphene (GR) are advantageous for their high surface area and unique electronic structure. Graphene is a network of sp^2 carbon atoms with a zero or very small band gap.[17] However, the bulk production and aggregation of graphene sheets prevent its mass usage in practical applications. GO and rGO are the oxidized counterparts of graphene, which can be produced easily. GO is a mixed network of sp^2 hybridized C–C bonds with sp^3 C–O bonds. The presence of oxygen groups results in a decrease in the conductivity of GO. In rGO, oxygen groups are removed and sp^2 hybridization is restored, resulting in the robustness of the material. The increased ratio of carbon to oxygen increases the conductivity of rGO sheets. Upon calcination at higher temperatures, the oxygen groups are completely removed to form GR, which shows outstanding conductivity.

In the present study, a comprehensive investigation of hydrogen spillover across diverse carbon supports, namely graphene oxide, reduced graphene oxide, graphene, and carbon black, is the focus to address the limited understanding of the spillover effect and its implications for hydrogen evolution reaction (HER) catalysis. To achieve this, we employed an efficient and cost-effective electrocatalyst, WO_3. Through systematic characterization and comparison of the catalytic performance exhibited by these carbon supports, we provide valuable insights into the underlying mechanisms of the spillover effect and its remarkable role in augmenting HER activity. Moreover, the stability in acidic and basic environments is detailed through Pourbaix 2D and 3D plots. Furthermore, the durability of the electrocatalysts is scrutinized for long-term stability tests and other electrochemical measurements in a free-standing carbon cloth substrate and SS substrate to realize the potential of the electrocatalyst for practical scalability. By expanding the knowledge base surrounding the utilization of carbon-based materials, our research paves the way for the development of alternative and cost-effective catalysts, thus presenting innovative approaches for the conversion of renewable energy. Furthermore, our study's emphasis on the spillover phenomenon and its correlation with HER activity addresses a crucial gap in the scientific literature.

2. Materials and methods

2.1. Reagents

Sodium tungstate dihydrate ($Na_2WO_4 \cdot 2H_2O$) (purity $\geq$ 99.9%), commercial Pt/C (20 wt%), and carbon cloth fibers (CC) were purchased from Sigma and used as received. Hydrochloric acid (HCl), oxalic acid, potassium hydroxide pellets (KOH), sodium chloride (NaCl), graphite flakes, carbon black, and absolute ethanol (99.9%) (C_2H_5OH) were procured from Hi-Media. Sulphuric acid (95–97% purity) (H_2SO_4) was purchased from Merck. Deionized (DI) water was used for the electrocatalyst synthesis and also for the preparation of catalyst ink and electrolyte solution.

2.2. Material synthesis

2.2.1. Synthesis of pristine hexagonal WO_3. The procedure incorporated to synthesize hexagonal WO_3 is a facile hydrothermal method. Into a solution containing 50 mL of DW, 1 M $Na_2WO_4 \cdot 2H_2O$ was introduced and stirred to attain a homogeneous solution. The pH of the solution was reduced to 1 using HCl solution. Before sealing the final solution in an autoclave, 3 g of Li_2SO_4 was added and the setup was maintained for 10 h at 180 °C. The final product obtained after cooling was washed several times with water and ethanol and dried at 100 °C overnight. Finally, to obtain hexagonal WO_3, calcination for 3 h at 450 °C was initiated.

2.2.2. Synthesis of carbon-based WO_3 electrocatalysts. Graphene oxide (GO) was prepared using graphite flakes by a modified Hummer's method reported earlier.[18] To derive reduced graphene oxide (rGO) from the synthesized GO, a chemical exfoliation technique was utilized where 20 mg of GO was dispersed along with 1 vol% of hydrazine hydrate solution and refluxed at ~100 °C for 2 h. The WO_3/GO electrocatalyst was synthesized by ultrasonication for 2–3 h with 20 mg of the synthesized GO powder with 80 mg of WO_3 nanorod powder sample. To prepare the WO_3/rGO electrocatalyst, the same amount of GO powder was introduced into a Teflon autoclave comprising the final homogeneous solution of WO_3 precursors and sealed for 10 h at 180 °C. The WO_3/GR electrocatalyst was further obtained by thermal expansion where the WO_3/rGO powder after washing and drying at room temperature was introduced into a quartz tube to attain a temperature of 300 °C along with argon gas purged into it. This splits the

reduced graphene oxide into multiple layers of reduced graphene sheets through the evolution of CO_2. The WO_3/CB electrocatalyst was obtained by ultrasonicating the specified amount of CB powder with the pristine WO_3 electrocatalyst as mentioned for WO_3/GO powder. To fabricate the CC@WO_3/GR electrode, carbon cloth fiber measuring 1 × 1 cm dimensions was introduced into the Teflon autoclave comprising the WO_3/GR precursor solution, and the above-mentioned protocol was repeated. To fabricate the SS@WO_3/GR electrode, the WO_3/GR powder electrocatalyst was made into a slurry using Nafion and ethanol and smeared on a SS substrate with the same 1 × 1 cm.

2.3. Physical characterization

Crystallographic information of the synthesized electrocatalysts was obtained by X-ray diffraction (XRD) (Rigaku Ultima IV X-ray Diffractometer with Cu-Kα radiation (λ = 1.5406 Å)). Raman spectra (Horiba Jobin Yvon, LabRam-HR Raman spectrometer) were obtained by using a 514 nm laser. Chemical surface composition and oxidation states were determined by XPS (ULVAC-PHI, PHI5000 Version Probe III). A field-emission scanning electron microscope (FEI, QUANTA 250-FEG) was used to observe the surface morphology. A TEM (JEOL, JEM-2100) and HR-TEM (JEOL, JEM-2100F) were utilized to investigate the structural information, chemical compositions, and elemental mapping of samples. The absorbance and bandgap calculations were performed by using a UV-vis spectrophotometer (UV-2550, Japan). The specific surface area and pore size distribution were interpreted using Brunner–Emmett–Teller (B–E–T) analysis (Microtrac, BELSORP-max).

2.4. Electrode preparation and electrochemical measurements

The preparation of catalyst inks includes 5 mg of ultrasonically dispersed catalyst into ethanol and Nafion solution (DuPont, 0.5 wt%) (8 : 2) ratio for 30 min. A catalyst loading mass of 0.36 mg cm^{-2} where 5 μL of catalyst inks (5 mg mL^{-1}) loaded onto a glassy carbon electrode GCE surface (3 mm in diameter) was pre-polished priorly with an exposed area of 0.07 cm^2.

Electrochemical measurements were performed with a PARSTAT electrochemical workstation in a standard three-electrode system comprising the respective electrocatalyst coated on a GCE/CC/SS substrate as the working electrode, a graphite rod as the counter electrode, and a saturated calomel electrode as the reference electrode. The electrolyte solutions taken for the study (0.5 M H_2SO_4, pH = 0 and 1 M KOH, pH = 14) were purged with Ar gas for 30 min before measurements. In all measurements, the potential was converted with respect to the Reversible Hydrogen Electrode (RHE) according to the Nernst equation:

$$E_{RHE} = E_{SCE} + E^{\circ}_{SCE} + 0.059 \times pH \quad (1)$$

where E_{RHE} describes the experimentally measured potential and E_{SCE} denotes the standard potential of the saturated calomel electrode.

For the cathodic measurements, ~50 CV cycles were performed to attain a stable polarization curve before each LSV curve was recorded. This pre-treatment helps to attain a stable polarization curve and ensures that the electrode surface is fully activated and that the electrolyte has reached steady-state conditions. The LSV curves for the powder electrocatalysts on the GCE were recorded in the potential range of −0.5 to 0.1 V *vs.* RHE at a sweep rate of 5 mV s^{-1} for both the electrolytes whereas for the electrodes using CC and SS, the potential range of −0.9 to 0.1 V *vs.* RHE at the same 5 mV s^{-1} scan rate. The stability tests were performed at their respective constant overvoltage values for a period of 16 h. The Tafel slope was obtained using the Tafel equation

$$\eta = b \log j + a \quad (2)$$

where η is the overpotential, b is the Tafel slope, a is the intercept and j is the current density in mA cm^{-2}. The turnover frequency was calculated using the relation

$$TOF = j/(m \times F \times n)\ (s^{-1}) \quad (3)$$

Here, j is the current density at a particular overpotential value (η in mV), m is the number of moles present in the catalyst, F is the Faraday constant (96 485.4C mol^{-1}), and n is the number of electrons transferred to generate one molecule of hydrogen gas which is 2. Electrochemical impedance spectra (EIS) were recorded at an overpotential from 0.1 Hz to 100 kHz with a modulation amplitude of 10 mV. The presented current density is normalized to the geometrical area of the GCE/CC fiber/SS substrate which is *iR*-corrected. To acquire the electrochemical active surface areas (ECSA), cyclic voltammograms at different scan rates were screened in the non-faradaic potential region and the roughness factor was determined according to the equation: ECSA = $R_f \times S$, where S is the geometric area of the electrode (here S is 1 cm^2). The R_f was determined by using $R_f = C_{dl}/40$ μF cm^{-2} based on the double-layer capacitance (C_{dl}) of a smooth oxide surface (60 μF cm^{-2}). The C_{dl} is extracted from the slope of $\Delta J = |j_a - j_c|$ *vs.* plots, where j_a and j_c represent the anodic and cathodic currents and ν is the scan rate.

3. Results and discussion

3.1. Physical characterization

Hexagonal WO_3 composited with carbonaceous materials (GO, rGO, GR, and CB) was synthesized from a single precursor to facilitate a strong contact between tungsten and carbon phases. Adopting the hydrothermal synthesis has paved the way for the unidirectional growth of WO_3 nanorods (Fig. 1d) with the highest aspect ratio of ~550 where, compared to the length (5.5–7.5 μm), the width is very negligible (100–200 nm). In the hydrothermal strategy, the addition of Li_2SO_4 resisted the nuclei's growth in the [110] direction and facilitated the progression in the [001] direction due to the adsorption of sulphate ions onto the WO_3 surface forming rod-like structures. The elemental composition and the spatial distribution of elements present in WO_3 nanorods were confirmed by EDAX and mapping (Fig. S1†). Integrating the 2D graphene-based

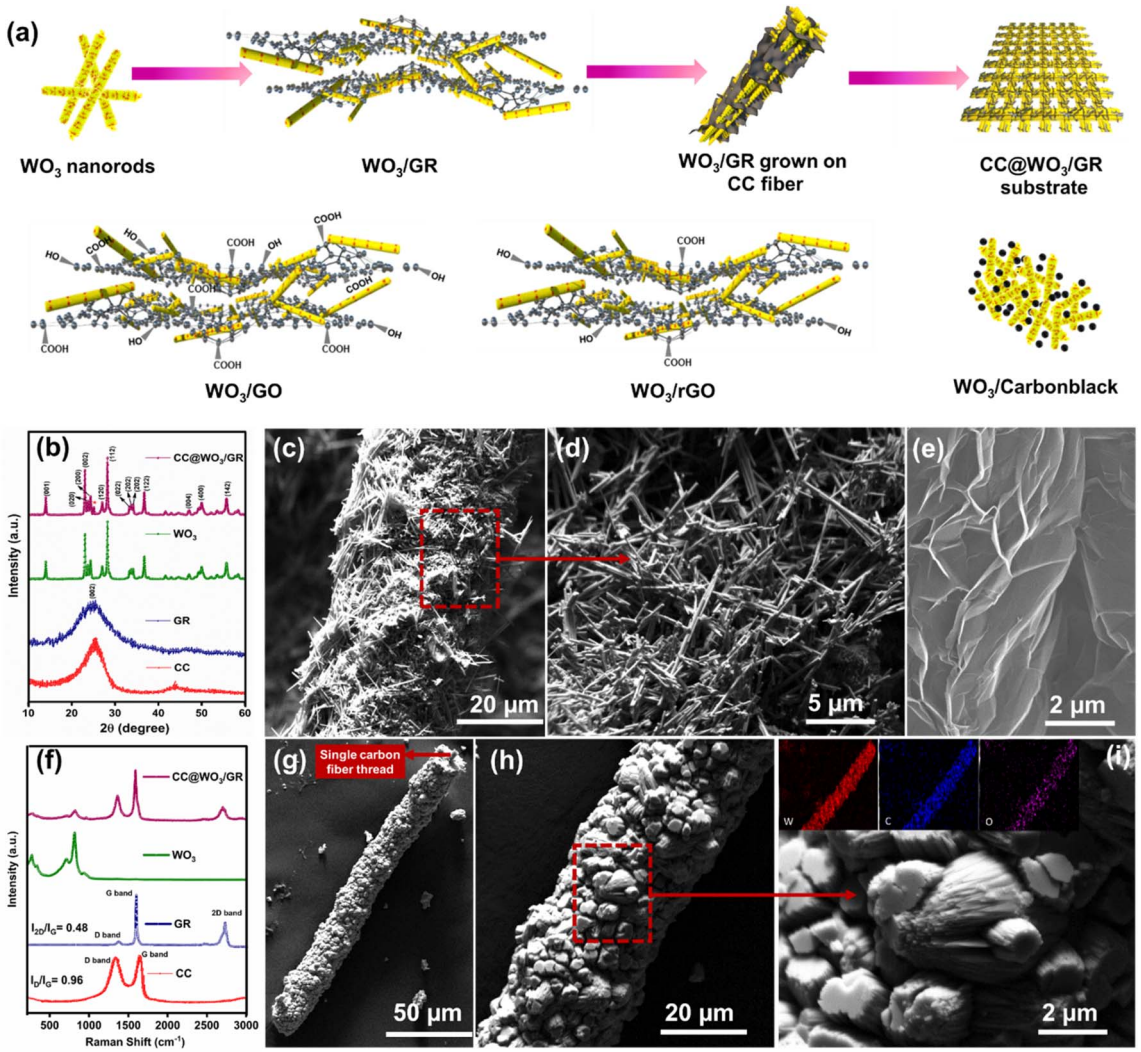

Fig. 1 (a) Schematic representation of hydrothermally synthesized WO_3/GO, WO_3/rGO, WO_3/GR, and WO_3/CB binary electrocatalysts and further fabrication of WO_3/GR on carbon cloth fiber (CC) to attain the CC@ WO_3/GR electrode, (b) XRD patterns of CC, reduced graphene sheets (GR), pristine WO_3 and CC@ WO_3/GR, (c) FESEM image of WO_3 nanorods grown on CC fiber, (d) the enlarged morphological analysis of WO_3 nanorods, (e) pristine graphene sheets screened through FESEM, (f) Raman spectra of CC, GR, pristine WO_3, and CC@ WO_3/GR, (g) the FESEM image of the WO_3/GR electrocatalyst grown on a single carbon fiber thread, and (h) and (i) the zoomed-in morphological view of WO_3 nanorods wrapped in graphene sheets with the respective elemental composition of W, C, and O in the inset of (i).

conducting species (GO, rGO and GR) and the sub-micro carbon black particles (CB) with the WO_3 metal oxide serves as a hot spot for water dissociation with a relatively low energy barrier of 0.81 eV.[19]

In the hierarchical fabrication of GO to rGO and GR from the parent compound graphite, the primary goal of the chemical exfoliation after the synthesis of GO from the modified Hummer's method is to utilize the hydrazine vapors to split the GO layers and reduce them to rGO. The rate of reduction is less compared to the thermal treatment that progressed after this step to procure reduced graphene sheets (GR). The rapid thermal treatment after the chemical exfoliation step is to enhance the interlayer spacing of rGO, thus creating wrinkled sheets of reduced graphene (Fig. 1e) with multiple layers having a high surface area compared to GO (Fig. S2†) and rGO (Fig. S3†).[20,21] Furthermore, the carbon content is also found to increase in the GR (Fig. S4†) compared to its counterpart rGO (Fig. S5†) due to the significant decrease in the oxygen functionalities. The FESEM image of the procured carbon black particles is depicted in Fig. S6.†

Hydrothermal synthesis incorporating carbon cloth (CC) as a substrate led to rod-like structures of hexagonal WO_3 being embedded in it as shown in Fig. 1c. It is worth mentioning that the incorporation of carbon cloth as a template for the growth of WO_3 nanocomposites with carbonaceous materials increases the electrical conductivity and also acts as a template for the practical implementation of catalyzing the hydrogen evolution reaction.[22] The reduced graphene (GR) composite of WO_3 nanorods on a CC substrate (CC@WO_3/GR) synthesized through a hydrothermal procedure has regulated an excellent blend of nanorods engulfed into the graphene multilayers leading to a convoluted structure with a high surface area

(Fig. 1g–i). Besides, the inset of Fig. 1i corresponds to the chemical maps of the elements W, C, and O monitored on the entire area of CC@WO_3/GR-scanned. The schematic illustration of the synthesis procedure of the CC@WO_3/GR electrode and the other nanocomposites of WO_3 is represented in Fig. 1a.

The X-ray diffraction peaks of pristine carbon cloth fiber (CC), pristine reduced graphene sheets (GR), hexagonal WO_3, and the electrocatalyst CC@WO_3/GR are depicted in Fig. 1b. A broad diffraction peak of carbon at 23° in XRD is resolved for both CC and GR denoting the (002) plane and an amorphous entity while pristine CC developed a peak at $2\theta = 44°$ signifying the (100) crystal plane of graphite.[23] The individual XRD patterns of rGO and CB (Fig. S7†) satisfy the basic (002) plane and the broader peaks reveal the amorphous nature of pristine carbon species while GO indicated a sharp peak at 11°. The pure hexagonal crystallographic plane intensities of pristine WO_3 matched well with the ICDD #01-075-2187 and the composite with graphene on CC fiber did not alter the crystallographic phase of WO_3.

Raman spectra are shown in Fig. 1f for the same set of samples as XRD. The spectrum of carbon cloth is similar to the graphene components (GO, rGO, and CB) illustrated in Fig. S8† comprising the D and G bands approximately at 1355 and 1594 cm^{-1} respectively. The I_D/I_G ratio increases in the order of 0.73, 0.94, 0.96, and 0.97 for CB, GO, CC, and rGO indicating a higher level of structural defects in reduced graphene oxide.[24] In the case of pristine reduced graphene sheets, the D band diminished and the development of a secondary peak known as the 2D band appeared at 2710 cm^{-1} with an I_{2D}/I_G ratio of 0.48 denoting multiple layers involved in GR.[23] In pristine WO_3, the δ (O–W–O) deformation vibrations were visible at 267 cm^{-1} and the ν (O–W–O) mode at 700 cm^{-1}. The band at 800 cm^{-1} is the distinguishing peak of h-WO_3 due to the WO_6 octahedra stacked in the 001 direction. The terminal W=O stretching mode is also visible at 915 cm^{-1}.[25] The CC@WO_3/GR composite contained all the respective baseline peaks where the G band and 2D band of the graphene layers were prominent.

To corroborate the surface compositions of WO_3/GO, WO_3/rGO, WO_3/GR, and WO_3/CB, XPS analysis was employed. The chemical states were determined by the deconvolution of W 4f, O 1s and C 1s using CasaXPS software implementing a Tougaard background. The baseline corrections were also employed. The full survey spectrum of all four composites is depicted in Fig. 2a confirming the presence of the elements W, O, and C in the nanocomposites. The XPS spectra of pure WO_3 are shown in Fig. S9a.† In the WO_3/GR nanocomposite, the high-resolution spectrum of the W 4f region (Fig. 2b) exhibits two major peaks at 35.36 eV and 37.5 eV, conforming the spin–orbit split levels – W $4f_{7/2}$ and W $4f_{5/2}$ of the W^{6+} oxidation state respectively. The low-intense peaks of W $4f_{7/2}$ and W $4f_{5/2}$ which

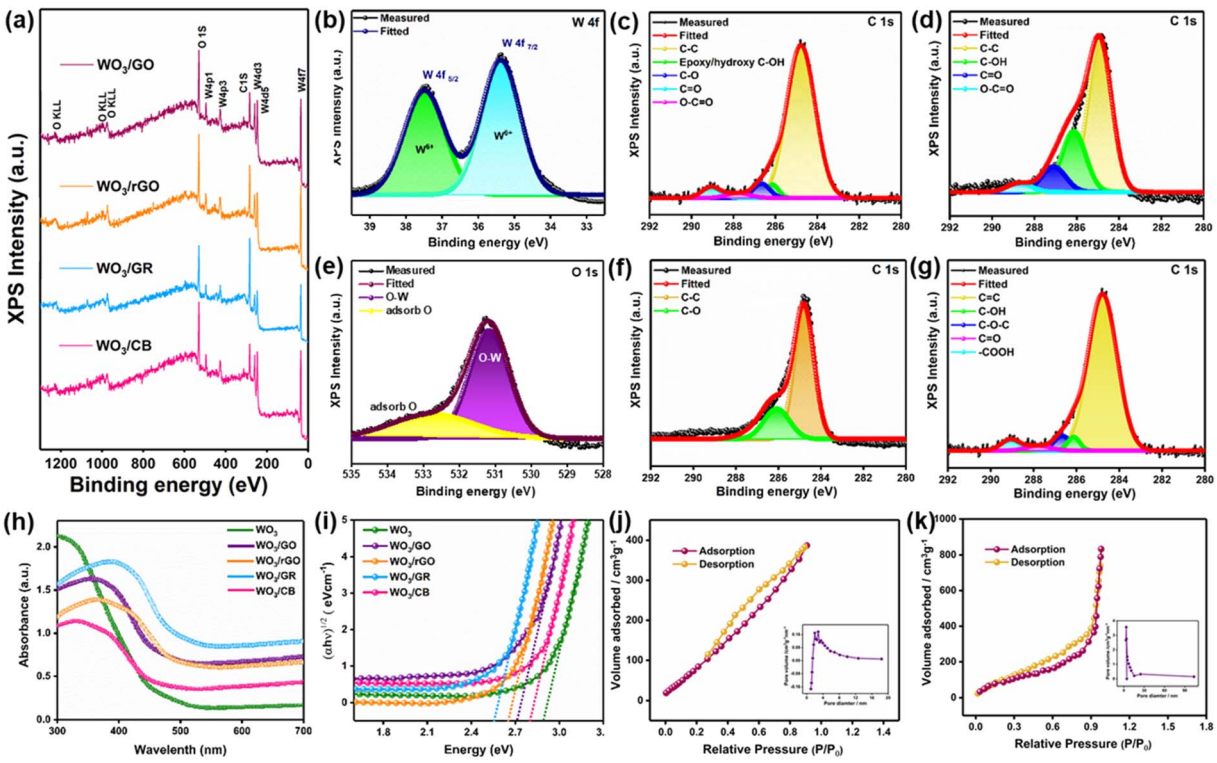

Fig. 2 (a) The XPS survey spectrum of WO_3/GO, WO_3/rGO, WO_3/GR, and WO_3/CB binary electrocatalysts. The high-resolution deconvoluted XPS spectra (b) W 4f of the WO_3/GR electrocatalyst, (c) C 1s of the WO_3/GO electrocatalyst, (d) C 1s of the WO_3/rGO electrocatalyst, (e) O 1s of the WO_3/GR electrocatalyst, (f) C 1s of the WO_3/GR electrocatalyst, and (g) C 1s of the WO_3/CB electrocatalyst. (h) The absorption spectra of the electrocatalysts from UV-visible spectroscopy, (i) Tauc plot calculated from the absorption spectra, and (j) and (k) the nitrogen adsorption–desorption isotherms of pristine WO_3 nanorods and the WO_3/GR composite respectively. Their respective BJH pore size distribution curves are depicted in the inset.

portray the W^{5+} oxidation state were also present in all four nanocomposites similar to pristine WO_3 (Fig. S9b†).[26] The latter confirms the successful incorporation of the carbon-based materials with the WO_3 structure highlighting the presence of substoichiometric entities of WO_3.

The oxygen 1s deconvoluted spectra of WO_3/GR (Fig. 2e) located at 530.47 eV relate to the lattice oxygen bonding with W while the peak at 532.17 eV corresponds to the chemisorbed oxygen species contributing to the surface groups in carbon-based materials. The surface oxygen groups of the graphene-based electrocatalyst were the least when compared to GO (Fig. S10a†), rGO (Fig. S10b†), and CB (Fig. S10c†). The results correlate with the carbon C 1s deconvoluted spectra (Fig. 2c, d, f and g) of each electrocatalyst indicating that the surface oxygen groups reduce as the reduction takes place from graphene oxide to reduced graphene sheets. Nevertheless, the area of the chemisorbed oxygen species in WO_3/CB was 5% greater than that of WO_3/GO hindering the conductivity. The oxygen content from XPS fitting was 36.95%, 28.96%, 22.64%, and 38.76% for WO_3/GO, WO_3/rGO, WO_3/GR, and WO_3/CB electrocatalysts respectively. The core level C 1s spectra of WO_3/GR (Fig. 2f) were localized at two binding energies of 284.82 eV and 286.09 eV reflecting the C–C and C–O while this was not the case in WO_3/GO (Fig. 2c), which yielded five deconvoluted peaks located at 284.7, 286.13, 286.64, 287.76, and 289.05 eV representing C–C, epoxy/hydroxy C–OH, C–O, O–C=O, and C=O respectively. In contrast, the spectrum of WO_3/rGO showed four bands 284.92, 286.14, 287.11, and 288.57 eV attributed to C–C, C–OH, C=O, and O–C=O respectively.[27,28] The oxygen functional groups kept decreasing when reduction occurred due to the chemical exfoliation and thermal treatment of GO. In the case of WO_3/CB, similar peaks of C–C advocate a binding energy of 284.80 eV, C–OH at 286.11 eV, and C–O–C at 286.65 eV, C=O at 287.79 eV, and–COOH at 289.03 eV respectively.[29] To conclude, during the reduction of GO, the majority of the residual oxides associated with a p-type conducting nature were converted to graphene, which when combined with the metal oxide WO_3 (n-type) can enable a conducting transition, increasing charge transfer across the p–n junction contact and consequently improving the reaction kinetics required for catalyzing the HER.[21,24,30]

The electronic interaction between the WO_3 and composites of GO, rGO, GR, and CB was investigated by UV-vis spectroscopy with their absorbance spectra shown in Fig. 2h. The absorbance wavelength of pristine WO_3 was 312 nm owing to the intrinsic bandgap absorption and the electronic transition between the filled O 2p orbital (valence band) and the empty 5d orbital (conduction band). When rGO is deduced from GO, a transition from sp^3 to sp^2 hybridization occurs with a bathochromic effect (redshift).[31] The absorption wavelength of WO_3/rGO was 371 nm compared to 358 nm for WO_3/GO. In contrast, the carbon black composite had a wavelength greater than WO_3 but less than the WO_3/GO hybrid appearing at 332 nm. The WO_3/GR composite exhibited the maximum absorbance wavelength of 386 nm indicating the effective composite formation of graphene sheets along with WO_3 leading to the inter-band charge transitions of WO_3. The band gap energy of the composites was calculated from the plot of $(\alpha h\nu)^{1/2}$ *vs.* $h\nu$, represented in Fig. 2i. The obtained band gap of pristine WO_3 was 2.89 eV, while it diminished to 2.79, 2.71, 2.65, and 2.55 eV for WO_3/CB, WO_3/GO, WO_3/rGO, and WO_3/GR respectively. The decrease in the bandgap predicts the defect states observed while the WO_3 is stacked into the rGO and GR compositions while these intermediate structures are absent in GO and CB compositions. The role of the surface area and pore size in catalyzing the hydrogen evolution reaction was investigated by the Brunauer–Emmett–Teller (B–E–T) and Barrett–Joyner–Halenda (B–J–H) methods. The specific surface area and the pore size distribution of pristine WO_3 and the WO_3/GR composite studied using adsorption–desorption analysis are depicted in Fig. 2j and k respectively. Both the samples showed type IV isotherms, indicating the mesoporous nature of particles with relative pressure. The specific surface area was the highest for the WO_3/GR nanocomposite exhibiting 138.71 $m^2\ g^{-1}$ with a pore size of 5.6 nm, which correlates well with the other obtained results. The pristine WO_3 nanorods exhibited a specific surface area of 109.13 $m^2\ g^{-1}$ with the least pore size of 3.8 nm. The incorporation of reduced graphene layers can significantly impact the porosity of the WO_3 nanorod as it acts as a scaffold, creating interconnected nanopores thereby increasing the overall porosity. This enhanced porosity contributes to the observed larger pore size of 5.6 nm. Also, the interaction between WO_3 nanorods and the two-dimensional hexagonal structure of graphene can promote the formation of mesopores (pores with diameters in the range of 2–50 nm) influencing the pore structure and modifying the crystal growth kinetics of WO_3, resulting in the formation of larger pores. The specific surface area of WO_3/GO, WO_3–rGO, and WO_3/CB nanocomposites was determined to be 120.79, 129.88, and 113.99 $m^2\ g^{-1}$, respectively. Consequently, the introduction of carbon and graphene derivatives into the WO_3 crystal structure could highly increase the specific area and deliver efficient adsorption and mass transfer of the hydroxyl radicals for the electrochemical reaction favorable for the hydrogen evolution reaction.[20,32]

The crystallinity and the evidence of composite formation were further confirmed by TEM and HRTEM analyses. Fig. 3a, c, e, and g show the TEM images of the hydrothermally synthesized WO_3/GO, WO_3/rGO, WO_3/GR, and WO_3/CB respectively. The interface between the graphene oxide and the 1D-WO_3 nanorod structures is clearly visible in Fig. 3a. The rGO layers from Fig. 3c revealed some void-like structures different from the plane sheet of GO indicating that reduction has taken place. The multilayer graphene sheets were visible on further reduction of rGO evident from Fig. 3e as the WO_3 nanorods were engulfed into the GR sheets implying that the intimate interfacial connection between them was intense.[33]

Nevertheless, the crystalline nature of the WO_3/GR composite was intact (Fig. 3e) compared to pure graphene sheets (Fig. S11†). However, the carbon black composite with WO_3 (Fig. 3g) showed an agglomerated composition of CB with WO_3. The HRTEM images of WO_3/GO, WO_3/rGO, WO_3/GR, and WO_3/CB are depicted in Fig. 3b, d, f, and h respectively, and their respective lattice fringes with the calculated interplanar spacing from inverse FFT evaluations are 0.374, 0.368, 0.364, and 0.379 nm respectively. The lattice fringes corresponded to

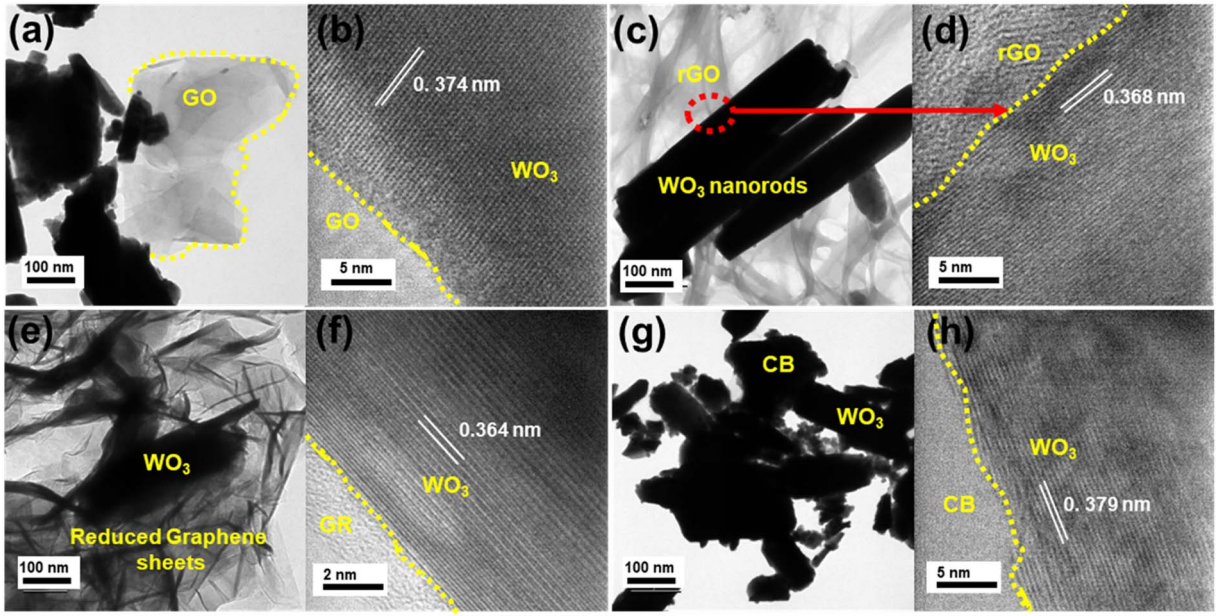

Fig. 3 (a) The TEM image of the WO_3/GO powder electrocatalyst and (b) HRTEM image representing the boundary of WO_3 with GO. The (c) TEM image and (d) HRTEM image of the WO_3/rGO powder electrocatalyst displaying the respective lattice spacing. The (e) TEM image and (f) high resolution TEM image representing the interplanar distance in nm and the boundary of WO_3 with GR layers and the (g) TEM image and (h) HRTEM image representing the lattice spacing of the WO_3/CB powder electrocatalyst.

the hexagonal WO_3 crystal phase with the crystallographic plane perpendicular to the nanorod axis having a consistent *d*-spacing of ~3.7 Å. This implies that the composite formation with the respective carbonaceous materials has not interrupted the lattice plane architecture and also the WO_3 crystal phase. Fig. S12† confirms the results obtained from FESEM with pristine WO_3 having a nanorod structure. The growth direction of WO_3 nanorods for the hexagonal phase is primarily in the [001] direction as the surface energy in the latter is much less than that of the [100] and the [110] facets owing to the abundance and compactness of the under-coordinated atoms of the [001] face.[34] Therefore, the geometric progression takes place in the same facet generating nanorods in the hexagonal phase.

3.2. Hydrogen evolution studies in acidic and alkaline media

To investigate the role of the incorporated carbonaceous materials – graphene oxide, reduced graphene oxide, reduced graphene sheets, and carbon black particles – into the hexagonal WO_3 crystal phase and to determine their overall efficacy towards catalyzing the HER, electrochemical measurements were designed and carried out using the same instrument with the consistent three-electrode set-up, electrolyte volume and accurate electrode positions. It is important to mention that primarily all five electrocatalysts – WO_3, WO_3/GO, WO_3/rGO, WO_3/GR, and WO_3/CB – were coated onto the GCE as mentioned in the electrochemical measurements section. Two different electrolyte solutions of extremely acidic 0.5 M H_2SO_4 (pH ~ 0) and extremely basic 1 M KOH (pH ~ 14) were considered for the study and linear sweep voltammetry (LSV) was employed to determine the onset potential and further calculate the Tafel slope of the respective electrocatalysts. The LSV measurements were carried out at a voltage swept from 0.1 to −0.5 V *versus* the reversible hydrogen electrode (RHE) at a scan rate of 5 mV s^{-1}. Fig. 4a and c show the *iR*-corrected polarization curves of the referred electrocatalysts and the standard catalyst for HER- Pt/C in acidic and alkaline electrolytes respectively. The overpotentials derived at a standard current density of 10 mA cm^{-2} and their slope values determined from the Tafel equation are depicted in Fig. 4e and g for acidic and basic electrolyte compositions respectively. Among all the synthesized samples, the WO_3/GR electrocatalyst possessed the least η@10 of 84 and 93 mV delivering the best HER catalytic activity with a Tafel slope of 66 and 72 mV dec^{-1} in 0.5 M H_2SO_4 and 1 M KOH respectively. The rationale behind the WO_3/GR electrocatalyst exhibiting superior HER activity can be ascribed to the delocalized π state bands initiating from the 2p orbitals spread over the carbon layer responsible for the sp^2 hybridization in the reduced graphene sheets.[21,31]

This facilitates better conductance of electrons when compared to rGO and GO. Graphene oxide due to its sp^3 hybridized carbon atoms with polar groups of chemically bonded epoxy, carboxyl, hydroxyl, and carbonyl in its basal pinacoid permits interfacial bonding for the enhancement of many functional properties. However, these polar oxygen functionalities when compared to pristine graphene are inferior in their physicochemical properties. The reduction of GO further eliminates these oxygen functionalities to transform into reduced graphene oxide and further thermal treatment produces reduced graphene layers of exceptional conductive properties.[35,36] However, as expected, the Pt/C (20 wt%) electrocatalyst surpassed all the other electrocatalysts with a striking overpotential of 15 and 17 mV and a Tafel slope of 29

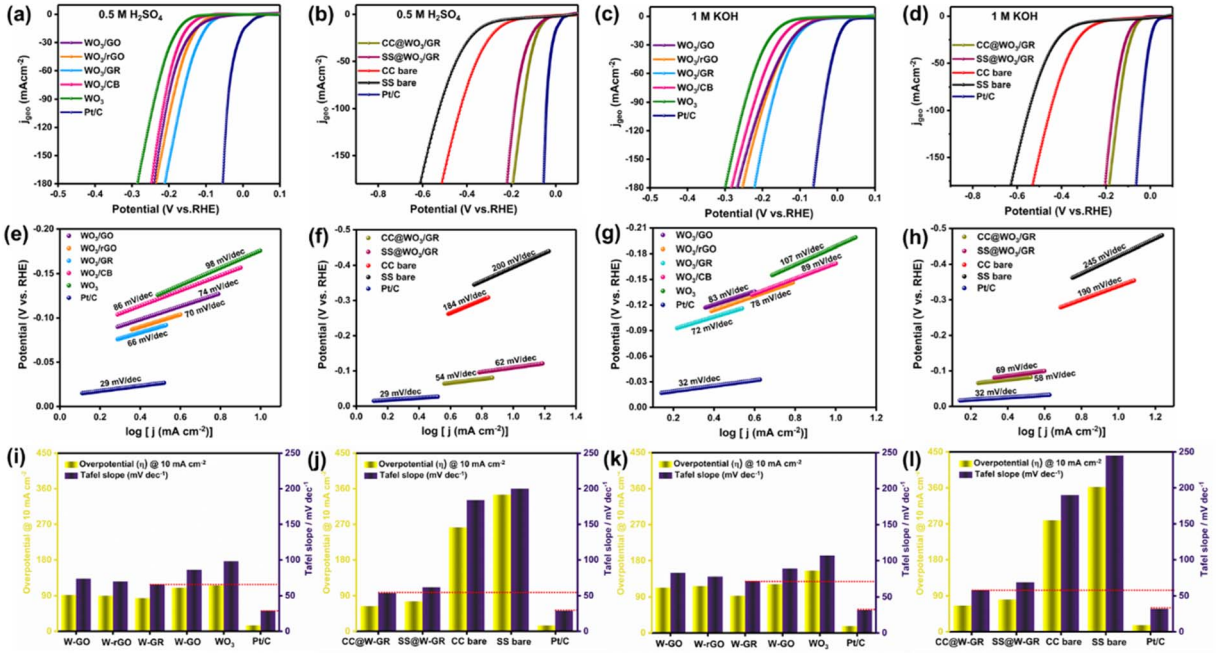

Fig. 4 The LSV polarization curves recorded for the (a) powder electrocatalysts in 0.5 M H_2SO_4, (b) the substrate (SS and CC) dependent WO_3/GR electrocatalyst in 0.5 M H_2SO_4, (c) powder electrocatalysts in 1 M KOH and (d) the substrate dependent WO_3/GR electrocatalyst in 1 M KOH respectively. The calculated Tafel slope of (e) powder samples coated on a GCE at pH = 0, (f) powder samples coated on substrates at pH = 0, (g) powder samples coated on a GCE at pH = 14 and (h) powder samples coated on substrates at pH = 14 respectively. Comparison of the onset potential measured at (η@10 mA cm^{-2}) and Tafel slope values in mV dec^{-1} for the (i) binary electrocatalysts in an acidic electrolyte, (j) substrate dependent electrocatalysts in an acidic electrolyte, (k) binary electrocatalysts in a basic electrolyte and (l) substrate dependent electrocatalysts in a basic electrolyte respectively.

and 32 mV dec^{-1} in acidic and alkaline electrolytes respectively. WO_3 nanorods displayed a high overpotential of 155 mV in the basic electrolyte whereas a relatively less η@10 of 116 mV in the H_2SO_4 electrolyte. Considering the composite formation of WO_3, the carbon black nanocomposite revealed the least potentiality towards hydrogen evolution with a Tafel slope of 86 mV dec^{-1} in 0.5 M H_2SO_4 compared to 66 mV dec^{-1} of the WO_3/GR electrocatalyst. This could be attributable to the bulk surface area,[37] thereby hindering the reaction kinetics compared to the 2D layered graphene entities. Glancing over the overpotential and Tafel slope values of all the studied electrocatalysts from Table S1† suggests that the catalytic activity towards the HER is more reliable in the acidic electrolyte than in the basic. The comparability of η@10 mA cm^{-2} and their respective Tafel slope values can be viewed in Fig. 4i and k for 0.5 M H_2SO_4 and 1 M KOH respectively.

As the preliminary studies on the catalysis of HER were performed on GCE, the practicality of the best WO_3 nanocomposite electrocatalyst – WO_3/GR was further deposited on two substrates – carbon fiber and stainless steel to investigate the real-time feasibility of the electrocatalysts for abundant hydrogen evolution. As predicted, the LSV polarization curves displayed in Fig. 4b and d are substantially better than the outcome from those lacking the substrates. The WO_3/GR electrocatalyst grown on carbon cloth fiber showed a striking Tafel slope of 54 and 58 mV dec^{-1} (Fig. 4f and h) with the onset potential, η@10 = 64 and 78 mV in 0.5 and 1 M KOH respectively. Nevertheless, the electrochemical performance of the SS counterpart was not as satisfactory as that of the CC substrate. This could be ascribed to the three-dimensional alignment of the binary electrocatalyst on the CC substrate, whereas the smearing of the WO_3/GR catalyst onto the SS substrate is only one-sided (two-dimensional) and hence fewer catalytic sites for the HER catalysis. The conductive capability of carbon cloth fiber with less resistance compared to SS also is an added advantage. The comparison of overpotential values *versus* their respective Tafel slope values of CC@WO_3/GR and SS@WO_3/GR in acidic and basic media is displayed in Fig. 4j and l respectively disclosing proximity to the Pt/C electrocatalyst. The instantaneous efficiency of the substrate-dependent electrocatalysts was scanned for the turnover frequency (TOF),[9] where at a maximum overpotential of 200 mV, a value of 0.561 and 0.524 s^{-1} was displayed by CC@WO_3/GR in pH = 0 and 14 respectively while the SS@WO_3/GR electrocatalyst exhibited a slightly lower response of 0.461 and 0.351 s^{-1} at pH = 0 and 14 respectively. The TOF of CC@WO_3/GR and SS@WO_3/GR in both the acidic and basic electrolytes at different overpotential values (50 to 200 mV) is displayed in Fig. S13† respectively. The overpotential values of all the electrocatalysts of WO_3 at different intervals of current density were assessed revealing that the acidic counterpart is more efficient for the hydrogen evolution reaction (Fig. S14†) than the basic.[38]

3.2.1. Mechanism of the hydrogen evolution reaction based on pH and surface chemistry of WO_3–carbon composites.

The mechanism underlying the process of hydrogen evolution upon the incorporation of the carbon black and graphene-based composites on hexagonal WO_3 is essential to unravel the kinetics involved in H_2 production. The hydrogen evolution reaction is a multistep approach involving intermediate mechanisms of adsorption, reduction, and desorption processes, which generates the diatomic gaseous hydrogen emanating from the surface of the working electrode. The elementary steps required to initiate the HER mechanism are classified mainly into three steps – the Volmer reaction refers to the adsorption of hydrogen from the respective electrolyte solution (as it differs in the case of acidic and basic conditions) and finally the recombination of the adsorbed hydrogen species *via* either the Heyrovsky or the Tafel mechanisms. The obtained Tafel slope of the electrocatalysts from the polarization curves also determines which two steps – either the Volmer–Heyrovsky or the Volmer-Tafel mechanism – have taken place. From Scheme 1b, it is clear that a Tafel slope of ~120 mV dec^{-1} denotes that the electrocatalyst has undergone the Volmer step, ~40 mV dec^{-1} represents the Heyrovsky step, and ~30 mV dec^{-1} signifies that the respective electrocatalyst has encountered the Tafel mechanism.[39] The pathways of the HER mechanism are intensely dependent on the catalytic activity at the electrode surface under extreme pH conditions and the equation of their respective Tafel slope is represented in Table S2.†

In an acidic environment, as the primary pathway for the commencement of the HER, a catalytic intermediate also called the adsorbed hydrogen atom (H_{ads}) is formed due to the coupling of an electron with an adsorbed proton on the active surface of the electrocatalyst. The proton source is the hydronium cation (H_3O^+) developed from the protonation of water. This step is referred to as the Volmer reaction. From here, the first probability is the transfer of an electron to an adsorbed hydrogen atom and further coupling with another proton from the Arrhenius acid molecules of the electrolyte solution to evolve H_2. This is termed the Volmer–Heyrovsky reaction *via* the electrochemical hydrogen desorption phenomenon. Another possible route is the recombination of two such H-intermediates *via* chemical desorption to evolve hydrogen. This is referred to as the combination or the Tafel reaction. The latter occurs only when the H_{ads} coverage is high which is applicable for high-end catalysts such as Pt while the Heyrovsky reaction occurs on a low H_{ads} exposure. In a basic medium, the Volmer process is initiated when a hydroxide ion and an adsorbed hydrogen species are released from the electrode surface as a result of the combination of water and an electron from the potential applied on the electrocatalyst. Two such adsorbed hydrogen atoms combine to evolve hydrogen aiming for the Tafel mechanism. Alternatively, another electron from H_2O may combine with the previously formed hydrogen species to release hydrogen gas molecules.[3,40] The mechanism of the hydrogen evolution reaction in acidic and basic electrolyte media is briefly illustrated in Schemes 1a and c respectively.

In distinction to these mechanistic insights into the HER, we could infer that all the synthesized binary electrocatalysts of WO_3 screened for HER catalysis in the electrochemical setup (Scheme 1d) follow the Volmer–Heyrovsky mechanism with the CC@WO_3/GR electrocatalyst bordering the Tafel mechanism and only the noble metal catalyst Pt/C trails the Volmer-Tafel mechanism and hence the least Tafel slope. The rate-

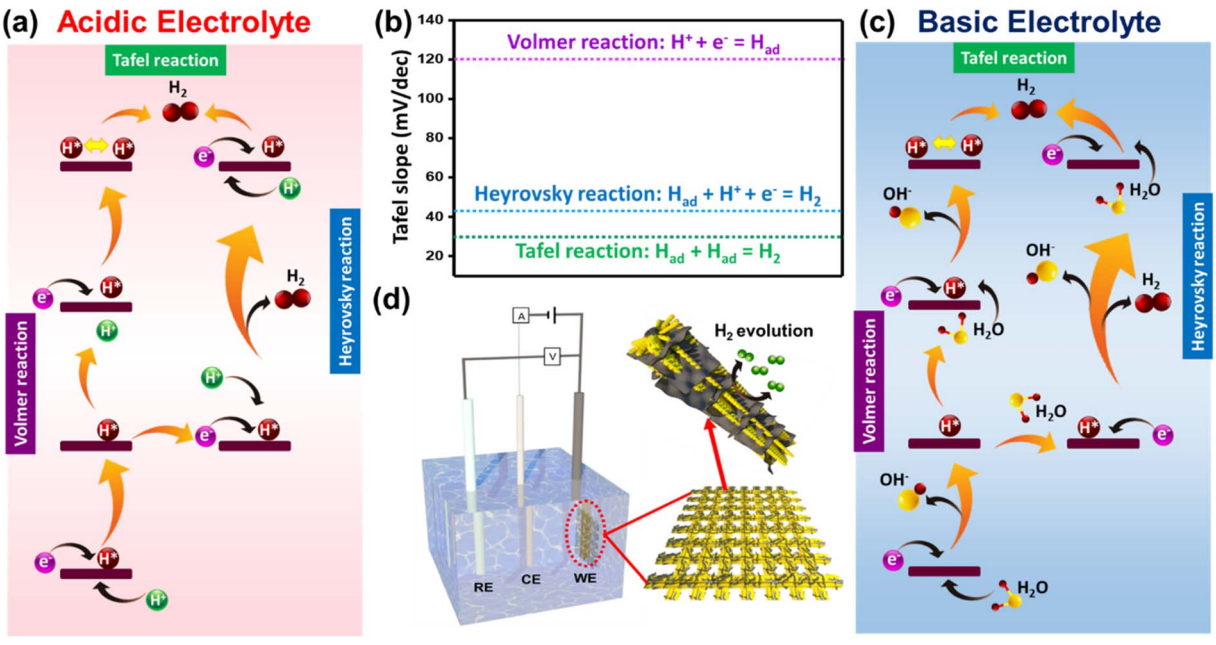

Scheme 1 Schematic illustration of the mechanism of the hydrogen evolution reaction representing the Volmer, Heyrovsky, and Tafel pathways in (a) an acidic electrolyte and (c) a basic electrolyte. (b) The hydrogen adsorption and desorption processes in the HER mechanism illustrated with their respective Tafel slope values and (d) the electrochemical step representing the working electrode – CC@WO_3/GR electrocatalyst for superior HER catalysis.

determining step is the Heyrovsky step ($H_{ad} + H^+ + e^- = H_2$) for all the synthesized electrocatalysts with the CC@WO_3/GR electrode showing no exception, but the Tafel slope value of the electrode is close to that of Pt/C indicating that the rate-determining step is the Tafel step ($2H_{ads} = H_2$).

3.2.2. Hydrogen spillover mechanism occurring in the WO_3/GR electrocatalyst. The hydrogen spillover effect (HSPE) is a phenomenon that occurs at the surface of an electrocatalyst where the decomposition of adsorbed hydrogen species from a metal surface is migrated to another hydrogen acceptor catalytic site (support) to generate hydrogen atoms. Concisely, the nature of the interaction between the hydrogen atoms and the support strongly influences the intrinsic kinetics of an electrocatalyst, altering the endurance and reactivity of a chemical reaction.[3,6,41] A broad overview of hydrogen spillover has recently emerged as a phenomenon of exceptional interest for understanding the underlying mechanism of the hydrogen evolution reaction,[41] especially in binary electrocatalysts consisting of a metal and support.[17,42] Several approaches have been previously designed to incorporate metallic Pt depending on whether it is hybridized with the parent component to enhance the HER performance through the hydrogen spillover mechanism.[5,43]

The conditions which favor the kickstart of the HSPE are primarily a metal surface capable of absorption of the dissociated hydrogen species from the electrolyte and secondly an acceptor for receiving the hydrogen species to act as a channel for hydrogen evolution. In our current investigation, the W atoms from WO_3 act as the metal component, and the graphene counterpart serves the purpose of an acceptor. The reduced graphene sheets in WO_3/GR with a disrupted 2D hexagonal ring structure (Fig. S15a–d†) form strong π–π interactions between the carbon framework owing to the domination of sp^2 hybridization over the sp^3 hybridized carbon atoms in the graphene oxide constituent of the WO_3/GO electrocatalyst.[21,24,31]

Fig. 5a illustrates the mechanism of the HSPE in different electrolyte media in the WO_3/GR binary electrocatalyst. The hydrogen spillover mechanism occurring in the binary metal

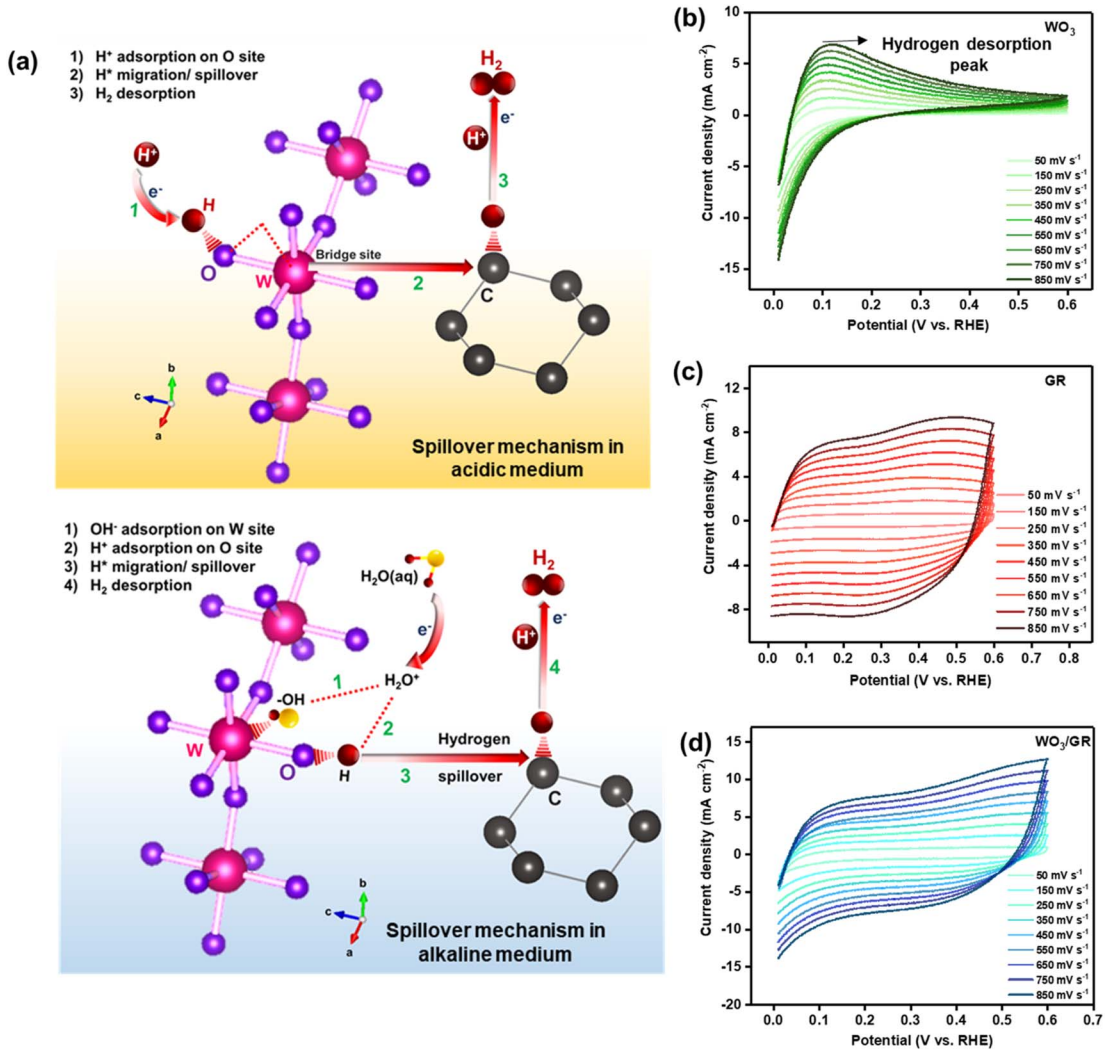

Fig. 5 (a) The illustration of the hydrogen spillover effect occurring at the atomic level of the WO_3/GR electrocatalyst in acidic and alkaline media and the cyclic voltammetry curves of (b) WO_3, (c) GR, and (d) WO_3/GR electrocatalysts at different scan rates indicating the hydrogen desorption peaks.

oxide and graphene supported WO_3/GR HER electrocatalyst could be attributed to three major milestones namely the proton adsorption followed by the migration of the proton also known as hydrogen spillover and finally the H_2 desorption. An important parameter called Gibbs free energy (ΔG_{H^*}) also evaluates the rate of hydrogen evolution where a negative value of ΔG_{H^*} favors the Volmer reaction and a high ΔG_{H^*} hinders the Heyrovsky or Tafel steps, thereby diminishing the pace of evolution at the surface of the electrocatalyst. An optimum ΔG_{H^*} value should be nearing zero for an active catalyst.[11,16] The adsorption process occurs in the metal, which in our case is tungsten metal when the $\Delta G_{H\text{-metal}} < 0$ favoring the hydrogen spillover from the metal to the support. The defective reduced graphene sheets having a $\Delta G_{H\text{-support}} > 0$ act as the support favoring interfacial hydrogen migration. The integration of both WO_3 and GR as the metal and support respectively stimulates both H^+ adsorption and H_2 desorption kinetically, thereby promoting the proton adsorption and hydrogen desorption as a strategy for the elimination of elements such as Pt while still delivering exceptional HER performance. The difference in the fermi energies between the metal (W) and the support (reduced graphene) enables them to create a Schottky junction at the interface of the metal and the support, which motivates the interfacial charge flow in the system.

The rate of the HSPE differs in the medium of catalysis (electrolyte) where the interaction between H^+ and OH^- species differs in the initial metal surface. From Fig. 5a, spillover in the acidic electrolyte initiates with H^+ adsorption, whereas OH^- adsorption occurs on the W site in the alkaline medium.[44,45] A bridge site is pronounced in 0.5 M H_2SO_4 at the W–O interface onto the defective graphene support, which favors H species to be spilled over to the accepting carbon support system. The catalytic process of the HSPE is thermodynamically feasible as the hydrogen atom which contains a proton and an electron migrates through the bridge site where the H^+ establishes a transitory chemical bond with the surficial carbon atoms and the electrons are diffused through the conduction band in the 2D graphene sheets. The desorption of H_2 occurs simultaneously assisting in the evolution of hydrogen gas molecules. In the case of an alkaline electrolyte, the adsorption process on the W (OH^-) and O (H^+) sites decelerates the reaction kinetics compared to only one adsorption site in the acidic electrolyte. Ultimately, this could be the possible reason for the higher overpotential and Tafel slope values of the WO_3 electrocatalyst with different carbon support systems in alkaline media compared to the acidic electrolyte. Furthermore, the adsorbed hydrogen atoms are spilled over by the HSPE forming C–H bonds on the graphene surface where desorption occurs to produce H_2. The number of C–H bonds formed also depends on the conductivity of the carbon support surface which is probably a potential explanation as to why the reduced graphene sheets surpassed the GO, rGO, and bulk CB counterparts in the rate kinetics of the HER with WO_3.

The experimental proof for the HSPE occurring in the WO_3/GR electrocatalyst and the level of the HSPE in different carbon-based supports (GO, rGO, GR, and CB) have been verified by electrochemical studies through CV at different scan rates indicating the hydrogen desorption curves of all the electrocatalysts in their pure and composition forms. The least slope value (Fig. 6a) of the hydrogen desorption curves was developed for the WO_3/GR electrocatalyst (Fig. 5d) compared to pure WO_3 (Fig. 5b) and pure reduced graphene sheets (Fig. 5c). When comparing the different carbon-based supports (GO, rGO, GR, and CB) (Fig. S16a–c†), the slope values were in the order of CB > GO > rGO > GR revealing that the HSPE occurs rapidly for the reduced graphene sheets (Fig. S16d†). The results have been correlated with previous studies on a Pt-based electrocatalyst.[45,46] To understand the HSPE through EIS spectroscopy, electrochemical impedance spectroscopy was carried out for the outstanding CC@WO_3/GR electrocatalyst in an acidic electrolyte medium at different overpotential values and is displayed in Fig. 6b. There were no prominent changes in the hydrogen adsorption resistance also known as R_2. Plotting $\log(1/R_2)$ *vs.* the overpotential values indicated a linear plot of the resistance values when plotted against the overpotential values. A lower slope value (also known as the Tafel slope calculated from EIS spectroscopy, according to Ohm's law) indicates that the hydrogen spillover reaction may have occurred rapidly due to the reduced graphene sheets as a composite with WO_3. The thermal stability profile of all four electrocatalysts WO_3/GO, WO_3–rGO, WO_3/GR, and WO_3/CB was investigated by thermogravimetric analysis (TGA) in the range of 30 °C to 850 °C at a rate of 10 °C min^{-1} to understand the HSPE. The TGA curve of all the electrocatalysts is depicted in Fig. S17(a)–(d).† The GO-based WO_3 composite showed an initial weight loss at around 122 °C depicting the evaporation of adsorbed water molecules from the GO network and around 220 °C describing the evolution of CO and CO_2 produced by the detachment of oxygen-containing groups from the GO surface and the weight loss around 500 °C can be assigned to the combustion of the skeleton of GO and almost no weight loss occurred above this temperature (Fig. S17a†).[28] In the case of other electrocatalysts based on rGO (Fig. S17b†) and CB (Fig. S17d†), the same trend followed but the pyrolysis of the carbon species might be different for rGO and CB compared to GO. Also, a stable environment for the rGO and the CB-based WO_3 electrocatalyst at temperatures 400–600 °C is seen after which the structure decomposes completely. Meanwhile, the WO_3/GR electrocatalyst (Fig. S17c†), after the initial weight loss after 100 °C, at around 300 °C and upwards the system undergoes a stable configuration indicating that the electrocatalysts can withhold higher temperatures and that the complete pyrolysis of the carbon skeleton structure along with WO_3 is decomposed only after 800 °C indicating excellent thermal stability of WO_3/graphene composite relating to the HSPE kinetics. Thermal stability plays a major role in ensuring the long-term stability and durability of the catalyst under ambient conditions. In the context of the hydrogen spillover effect, the thermally stable WO_3/GR electrocatalyst can be advantageous, as it can maintain its structural integrity and retain its catalytic activity over extended periods. This allows for consistent and reliable performance of the catalyst in HER catalysis. Moreover, even at room temperature, the presence of thermal fluctuations and localized heating effects due to the catalytic reaction itself can

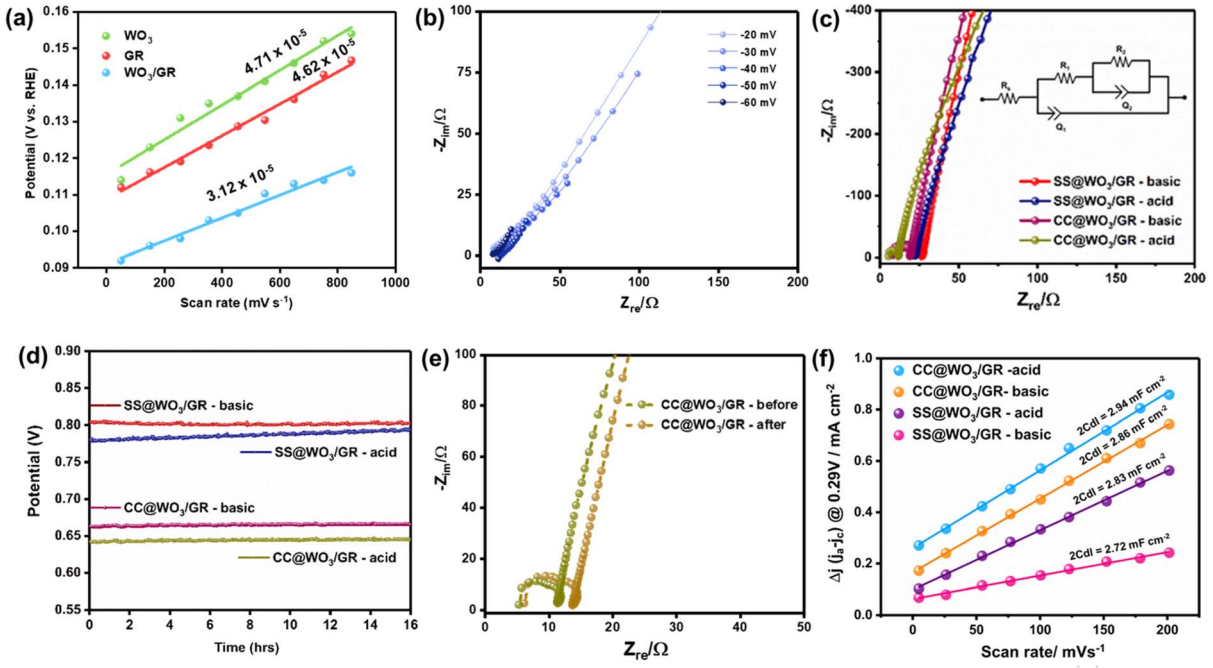

Fig. 6 (a) The slope values of the desorption peak at different potential values *vs.* the scan rate values to determine the slope values of WO_3, GR, and WO_3/GR, (b) electrochemical impedance spectroscopy of the WO_3/GR electrocatalyst at different overpotential values, (c) the EIS Nyquist plot of CC@WO_3/GR and SS@WO_3/GR electrocatalysts in 0.5 M H_2SO_4 and 1 M KOH electrolytes (inset represents the equivalent circuit model), (d) the chronopotentiometry analysis of CC@WO_3/GR and SS@WO_3/GR at extreme pH values for a prolonged duration of 16 h at a current density of 10 mA cm^{-2}, (e) the electrochemical impedance spectroscopy of CC@WO_3/GR before and after the stability test and (f) the capacitance obtained from the fit of double-layer charging current density *versus* scan rate for CC@WO_3/GR and SS@WO_3/GR in acidic and basic electrolytes respectively.

result in temperature gradients on the catalyst surface. In such cases, the WO_3/GR electrocatalyst when compared to the other electrocatalysts will be less prone to undergoing structural modifications or deterioration under these conditions, ensuring the stability of the catalyst's performance during the HER for the HSPE.[39,47] The DTA peaks of all the carbon-based electrocatalysts indicate that the reaction that occurred is exothermic.

Reports suggest that the spillover distance in single-atom electrocatalysts (such as $La_2Sr_2PtO_{7+\delta}$)[45,46] is usually very short, typically on the order of a few angstroms (Å), due to the strong interaction between the hydrogen molecule and the metal atom. However, the spillover distance in heterogeneous catalysts such as WO_3/graphene may be longer due to the presence of multiple active sites and the diffusion of hydrogen molecules through the graphene matrix. It is worth noting that the exact spillover distance between WO_3 and graphene may depend on various factors such as the morphology of the WO_3 nanorods. As the nanorods have been engulfed into the graphene layer structures as depicted in Fig. 1(g)–(i), the WO_3/GR nanocomposite is considered a single entity which proves that the distance between the WO_3 and graphene interface is minimal for the HSPE to occur but definitely greater than that of single atom electrocatalysts. The exceptional HER catalyzing performance of CC@WO_3/GR is expected to originate from the strong physico-chemical and electronic coupling between the metal oxide, the graphene layers, and the conducting CC substrate. The unidirectional WO_3 nanorods were merged into the graphene layers (Fig. 1i) resulting in the availability of numerous edges that could serve as active sites for catalyzing the HER. The electron diffusion to the reduced graphene layers in a cohesive conductive system was ensured by the high resistance of WO_3 nanorods in the electrode.

To analyze these interactions, electrochemical impedance measurements (EIS) were performed on the electrodes in the frequency region of 10^6 to 0.1 Hz at an amplitude of 10 mV. As depicted in Fig. 6c, the faradaic impedance and the solution resistance of CC@WO_3/GR in 0.5 M H_2SO_4 solution were the least when compared to the stainless steel substrate in both the acidic and alkaline electrolytes (Fig. S18†) with a capacitive behavior denoted by the straight line in the low-frequency region. This establishes extraordinary electrocatalysis kinetics which manifests the conductive capability of the electrocatalyst.[42,48] The inset represents the respective electrical equivalent circuit diagram. The circuit model with which the EIS data were fit is represented in the Fig. 6c inset. In the equivalent circuit, one parallel R‖C circuit is embedded within a second parallel R‖C circuit. Q_2 represents the capacitance of the surface layers between WO_3 and the graphene sheets including any defect states, whereas Q_1 represents the bulk capacitance of the WO_3 nanocomposite. When $Q_1 \gg Q_2$, the circuit model resembles Randle's circuit with a single arc in the Nyquist plot as represented in Fig. 6c. In such a case, the total resistance is $R_1 + R_2$ called as the charge transfer resistance

(R_{ct}).[49] The value of R_{ct} is the least (5.88 Ω) for the CC@WO_3/GR electrocatalyst in the acidic media and the parameter R_s represents the solution resistance which is $R_s = 5.18$ Ω for the same electrocatalyst. The least R_s and R_{ct} values indicate better conductivity and the ion transfer mechanism at the electrode–electrolyte interface occurs at a faster pace. The cut-off frequency (f_c) (Fig. S19a†) and the shift in the phase angle (Fig. S19b†) are also negligible for the carbon cloth supported WO_3/GR electrocatalyst revealing good capacitive behavior of the electrode. The evaluation of the solution resistance, charge transfer resistance, frequency cut-off, and phase angle of the most capable CC@WO_3/GR electrocatalyst (Fig. S20†) indicate that the stability and robustness of charge transfer kinetics are more reliable in acidic media than in basic electrolytes. The chronopotentiometric curves from Fig. 6d revealed a stable progression of the graphene-based WO_3 electrocatalyst fabricated on carbon cloth fiber in both the acidic and alkaline electrolytes at a specified scanned period of 16 h indicating consistent delivery of hydrogen bubbles from the active catalytic sites.[7,42,50] The EIS data of the well-performed CC@WO_3/GR electrocatalyst in the 0.5 M H_2SO_4 electrolyte were obtained after the long stability test for 16 h and are displayed in Fig. 6e. The solution resistance was not altered much and remained at 5.46 Ω but the charge transfer resistance R_{ct} was increased to 7.4 Ω which indicated that the resistance to charge transfer between the metal oxide and conductive substrates increased as the active sites required for the reaction kinetics have been passivated after the chronopotentiometric studies. Nevertheless, the performance of the SS@WO_3/GR electrode tends to become less stable as the potential is seen to increase in the acidic electrolyte media which may be due to the metallic properties of the SS substrate that leads to etching of the electrode substrate interface.

To catalyze the hydrogen evolution reaction, the electrochemical performance of the electrodes was also evaluated by determining their electrochemically active surface area (ECSA). The cyclic voltammograms of SS@WO_3/GR and CC@WO_3/GR in two electrolyte media at different scan rates in the non-faradaic region are presented in Fig. S21.† The calculated double layer capacitance ($2C_{dl}$) derived from the slope of plotting $\Delta J = J_a - J_c$ *versus* the screened scan rates is displayed in Fig. 6f. As predicted, a maximum capacitance of 2.94 mF cm^{-2} (ECSA = 36.75 cm^{-2}) was delivered by the CC@WO_3/GR electrode in 0.5 M H_2SO_4 solution with the SS@WO_3/GR electrode demonstrating the least capacitance of 2.72 mF cm^{-2} (ECSA = 34 cm^{-2}). The findings suggest that more active sites are accessible from the electrochemical surface area for efficient charge transfer necessary for HER catalysis.[51] The ECSA values were also derived for the powder electrocatalysts of WO_3/GO, WO_3/rGO, WO_3/GR, and WO_3/CB in the non-faradaic region and are presented in Fig. S22(a)–(d).† Their difference in the slope values from the anodic and the cathodic values at 0.29 V depicted that the electrochemically active surface area is in the order of 24.75 < 19.75 < 17.75 < 16.75 cm^{-2} for the electrocatalysts in the order WO_3/GR < WO_3/rGO < WO_3/GO and WO_3/CB respectively with their respective $2C_{dl}$ values presented in Fig. S23.† To compare the specific activity of the electrocatalysts WO_3/GO, WO_3/rGO, WO_3/GR, and WO_3/CB with respect to the electrochemically active surface area (ECSA), the polarization curves of LSV were normalized by ECSA values (Fig. S24a†) instead of the geometric surface area (Fig. 4a) in the acidic electrolyte medium. Fig. S24b† represents the difference in the overpotential values from the normalized geometric surface area and the ECSA depicting that the overpotential is the least for the ECSA normalized values.

To illustrate the intermediate possibilities of electrochemical processes involved in WO_3 and their nanocomposite formation with carbon derivatives influenced by the pH of the electrolyte, a stability profile known as the Pourbaix diagram was employed. The Nernst equation was used (see eqn (4)), to illustrate the Pourbaix plot represented by the pH on the *x*-axis *vs.* the reduction potential Eh (V) on the *y*-axis.[7] The E–pH plot was constructed by monitoring the concentration of soluble species of all elements (W and C) at 1 e^{-8} mol kg^{-1} and 298 K. In the stability plot, the electron transfer reactions which are pH-insensitive but voltage-dependent are represented by the horizontal lines; however, the vertical lines are potential-independent but pH-dependent, with no electron transport.

$$E = E^{\circ} - \frac{RT}{zF}\ln\frac{a_{Red}}{a_{Ox}} \quad (4)$$

Fig. 7a depicts the Pourbaix stability profile (E–pH) of water where no other metal elements are involved. Considering that no overpotential is involved, the equilibrium conditions above the top line involve oxidation of water where oxygen gas bubbles evolve from the electrode represented by eqn (5) and below the bottom line involve hydrogen ions reacting with the electrons to produce hydrogen gas represented by eqn (6). Water is thermodynamically stable and no gas is generated for the potential and pH values between lines.[50]

$$2H^+ + 2e^- \rightarrow H_2 \quad (5)$$

$$O_2 + 4H^+ + 4e^- \rightarrow 2H_2O \quad (6)$$

Fig. 7b contains the essential information demonstrating the stability of WO_3 in terms of the E–pH plot with the concentration at 1 e^{-8} mol kg^{-1} of the soluble species. As seen in the figure, the location of the stability limits for the WO_3 falls in the lower pH region, while the tungstate ions (WO_4^{2-}) and the polytungstate ion ($HW_6O_{21}^{5-}$) species dominate the neutral and alkaline pH values respectively. The reflection of tungsten's Pourbaix stability shows that it is corrosion resistant when the potential is adjusted below Eh = −1.2 V suggesting that the capacity of WO_3 under acidic conditions is stable enough to evolve hydrogen gas molecules below the specified voltage.[52]

The reactions specifying the Nernst equations required to construct the 3D Pourbaix diagram as a function of pH (*x*-axis), potential Eh (*y*-axis), and the log of concentration C (*z*-axis) are represented in Table S3† and illustrated in Fig. 7d respectively. Carbon's Pourbaix diagram from Fig. 7c suggests that it is thermodynamically unstable over the alkaline range of pH due

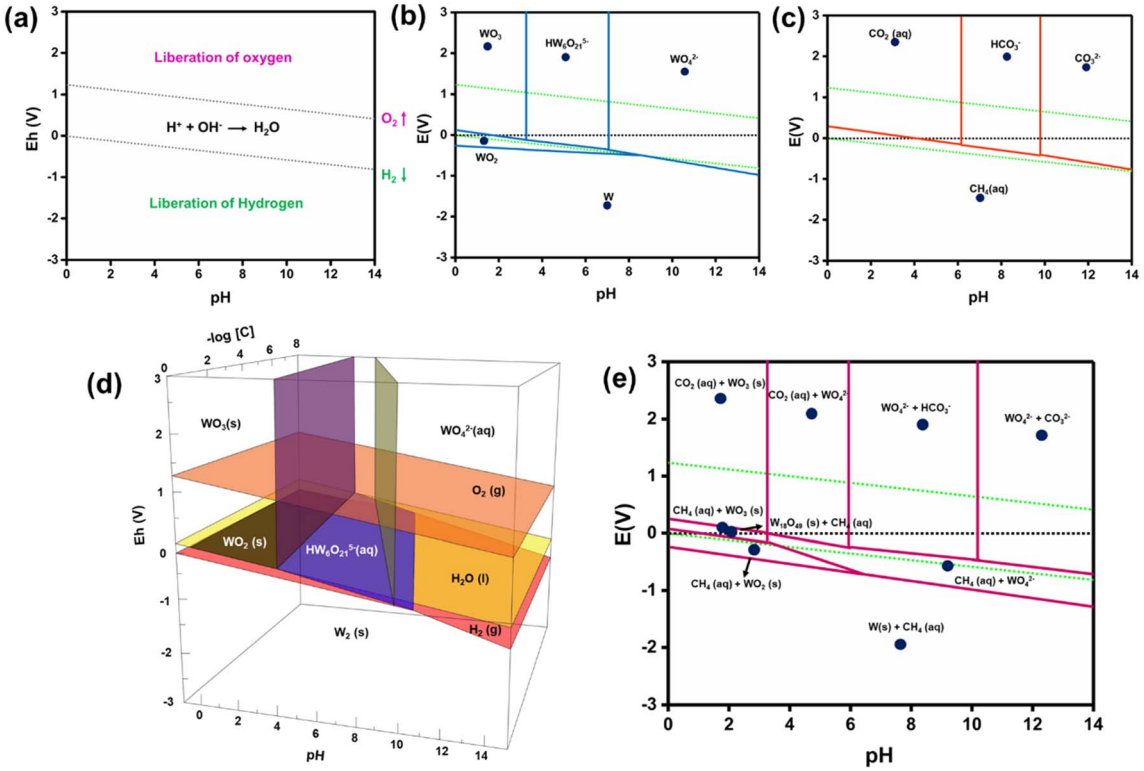

Fig. 7 (a) The Pourbaix stability profile of water signifying the hydrogen and oxygen evolution potentials. The two-dimensional Pourbaix diagram (Eh–pH) of (b) WO_3 and (c) carbon with the concentration of the soluble species at 1 e^{-8} mol kg^{-1} and the temperature at 298 K. (d) The 3D Pourbaix stability profile (Eh–pH-C) of WO_3 comprising the stability boundaries of water and (e) the Eh–pH plot of the WO_3/graphene composite at 1 e^{-8} mol kg^{-1} concentration and 298 K representing their stable and unstable entities.

to its inherent corrosion potential. To favor the hydrogen evolution reaction, the H^+ ions should be absorbed, as protonation is necessary to maintain the equilibrium potential as well as to catalyze the HER in acidic circumstances. Carbon requires four electrons (oxidation state of +4) to result in an oxide that is hindered under acidic conditions by high activation energy barriers. An increase in HER activity was associated with an excess of protons at low pH levels. Nevertheless, the alkaline environment requires the formation of OH^- ions rather than the consumption of H^+ ions. Considering both cases, water functions as a proton donor for the latter. The standard electrode potentials regarding the carbon are specified from eqn (7)–(13) *versus* the SHE (standard hydrogen electrode) at 25 °C and pH = 7.

$$C + 2H_2O \leftrightarrow CO_2 + 4H^+ + 4e^-,\ E^\circ = -0.118\ V\ vs.\ SHE \quad (7)$$

$$C + 6OH^- \leftrightarrow CO_3^{2-} + 3H_2O + 4e^-,\ E^\circ = -0.854\ V\ vs.\ SHE \quad (8)$$

$$CO_2 + H_2O + 2e^- \leftrightarrow HCOO^- + OH^-,\ E^\circ = -0.43\ V\ vs.\ SHE \quad (9)$$

$$O_2 + H_2O + 2e^- \leftrightarrow CO + 2OH^-,\ E^\circ = -0.52\ V\ vs.\ SHE \quad (10)$$

$$CO_2 + 6H_2O + 8e^- \leftrightarrow CH_4 + 8OH^-,\ E^\circ = -0.25\ V\ vs.\ SHE \quad (11)$$

$$O_2 + 8H_2O + 12e^- \leftrightarrow C_2H_4 + 12OH^-,\ E^\circ = -0.34\ V\ vs.\ SHE \quad (12)$$

$$O_2 + 9H_2O + 12e^- \leftrightarrow C_2H_5OH + 12OH^-,\ E^\circ = -0.33\ V\ vs.\ SHE \quad (13)$$

The most striking observation to emerge from the E–pH plot (Fig. 7e) when elements W and C were interpreted in the ratio of 80 : 20 was that the phase domains were not electrochemically stable at high alkalinity. Although the corrosion properties of carbon are not well appreciated due to their nucleophilic nature, producing OH^- ions in alkaline environments owing to oxidation, the situation was ameliorated when reacted with WO_3 as it produced solid and stable electrochemical phases under acidic conditions compared to the aqueous and unstable electrochemical species in high alkalinity environments.[5,11,44] The oxidation of WO_3 is combined with the formation of CO_2 species whereas the reduction potential is in proximity to the reduction potential of water giving rise to methane in the aqueous form which further reduces to form hydrogen gas molecules when reacting with H_2O.[53] There are many other stable and unstable species (Table S4†) when tungsten combines with carbon in the vast pH range of electrolyte solutions.

To evaluate the HER durability and stability of the CC@WO_3/GR electrode for scalable applications, chronoamperometric measurements were performed sequentially for over 16 h in a high concentration acidic solution (0.5 M H_2SO_4). The electrocatalytic stability at various current densities (10, 50, 100,

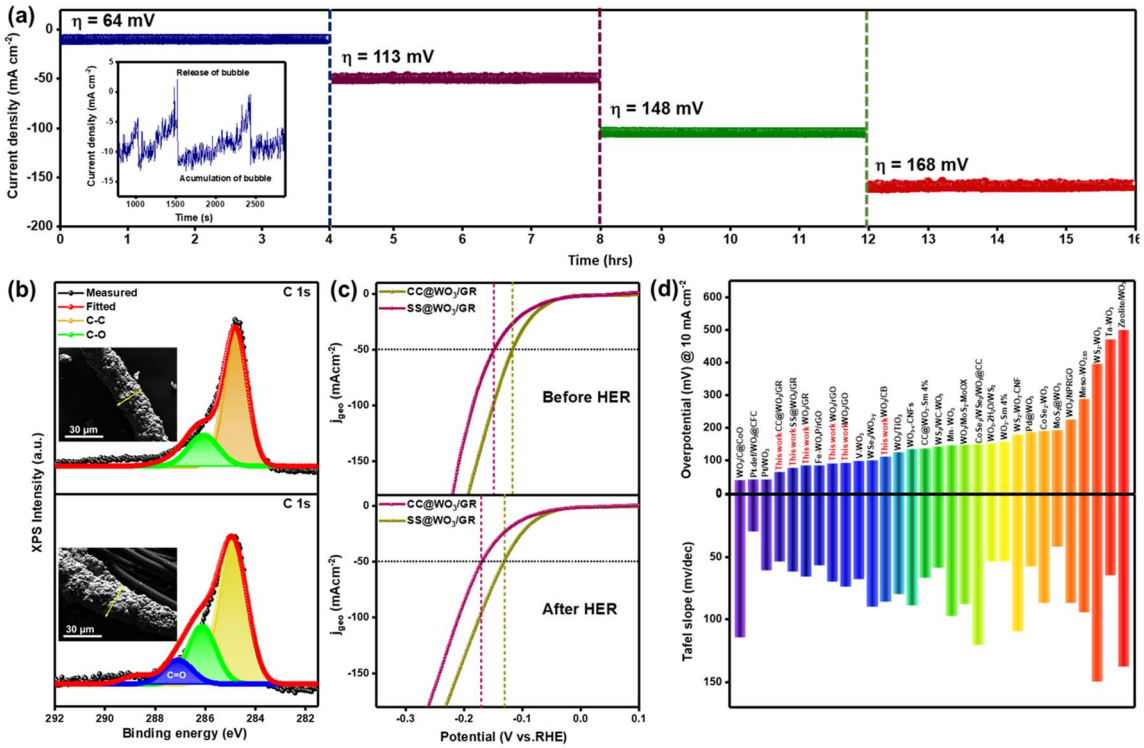

Fig. 8 (a) Chronoamperometric measurements for a prolonged interval of time at different current densities under their respective static overpotentials for the CC@WO_3/GR electrocatalyst in 0.5 M H_2SO_4. The inset represents the varying peak position of the release and the accumulation of H_2 bubbles, (b) XPS analysis and the deconvoluted spectra of C 1s in CC@WO_3/GR before and after the HER catalysis. The inset represents the before and after FESEM images of the electrocatalyst, (c) the LSV polarization curves of CC@WO_3/GR and SSWO_3/GR electrocatalysts before and after the long-term stability assessment, and (d) the comparison of overpotential values at 10 mA cm^{-2} and the Tafel slope for all the synthesized and fabricated electrocatalysts (WO_3/GO, WO_3/rGO, WO_3/GR, WO_3/CB, CC@WO_3/GR and SS@WO_3/GR) with a previous WO_3 based electrocatalyst for catalyzing the HER.

and 150 mA cm^{-2}) was investigated using chronoamperometry at their respective static overpotentials η = 64, 113, 148, and 168 mV obtained from Fig. 4b respectively. As depicted in Fig. 8a, the current densities were stable at their respective overpotential values for a concurrent period of 4 h. It is visible from the inset image of the enlarged stability analysis that the rise in the peak implies the release of the bubble and the drop of the peak resembles the accumulation of the H_2 bubble at the surface.[54] Furthermore, the electrocatalyst was screened for XPS and FESEM after the chronoamperometric assessment and the CC@WO_3/GR electrode exhibited satisfactory structural stability with a slightly bulged morphology (Fig. 8b inset) with no obvious change in the surface structure indicating that the catalyst has undergone oxidation, which is consistent with the XPS outcome.[25,52,55,56] When a portion of the electrocatalyst was scanned for morphological analysis (Fig. S25†) after the stability test, results expose the intact nature of the WO_3/GR composite onto the carbon fiber substrate indicating good adherence of the electrocatalyst onto the substrate even after long hours of electrochemical tests. The XPS analysis reveals that W (Fig. S26†) and O (Fig. S27†) atoms retain their respective oxidation states with a slight decrease in their peak intensities indicating that the atomic concentration is decreased with more H_2 generation. Consequently, the LSVs recorded after the long-term stability test (Fig. 8c) implied that CC@WO_3/GR at 50 mA cm^{-2} decayed only 2.4%, whereas the SS@WO_3/GR electrode decay percentage was 12.5%. The fabricated CC@WO_3/GR electrode and the other electrocatalysts in our work were extensively compared (Fig. 8d) with previously reported WO_3-based catalysts (Table S5†) for their HER kinetics (Tafel slope and overpotential (η@10) values) and the data reveal that they are the best among the compared HER catalysts without noble metal (Pt) doping. The aforementioned results emphasize that the compositional engineering strategy of the binary electrocatalysts in our work provides an avenue to enhance the performance of HER catalysis in a wide pH range and more especially in an acidic environment.

4. Conclusion

In conclusion, our study focused on the development of a three-dimensional flexible electrode incorporating a binary nanocomposite of hexagonal unidirectional WO_3 nanorods and reduced graphene layers aligned on a conductive carbon fiber substrate. The performance of various carbonaceous supports, including graphene oxide (GO), reduced graphene oxide (rGO), carbon black (CB), and WO_3/GR electrocatalyst, was evaluated in terms of the hydrogen spillover effect (HSPE). Among the investigated carbon supports, WO_3/GR exhibited the highest HSPE. This was evident from the significantly lower

overpotentials of 64 and 78 mV, at a current density of 10 mA cm^{-2}, and excellent Tafel slopes of 54 and 58 mV dec^{-1} in acidic and basic electrolyte environments, respectively. A current density of 100 mA cm^{-2} was achieved by the CC@WO_3/GR electrode two fold less than that of the CB binary composition at a low overpotential of 150 mV ensuring excellent durability and a stable potentiostatic profile for extended hours of practicality. Our findings indicate that the intrinsic activity of the multifunctional active sites within the CC@WO_3/GR electrode plays a crucial role in facilitating the HSPE. The proton adsorption in the O site, combined with W acting as a mediator for hydrogen spillover to the carbon support, promotes the release of H_2 gas through the desorption process, particularly in acidic media. The HSPE has also been observed in various electrochemical studies on carbon-based electrocatalysts, further confirming the effectiveness of this mechanism. Based on the observed performance, we can rank the carbonaceous supports in terms of the HSPE as follows: WO_3/GR > rGO > GO > CB. The stability of CC@WO_3/GR is also impressive in the alkaline electrolyte thereby opening new avenues for scaling the 3D binary electrocatalyst for industrial hydrogen production more economically and efficiently.

Conflicts of interest

The authors declare that they have no known competing financial interests or personal relationships that could have appeared to influence the work reported in this paper.

Acknowledgements

The authors thank the DST-SERB for the funding [EMR/2016/007676] as well as the DST-FIST, DST-PURSE, UGC-SAP, and the Government of India for the support of instrumental facilities available in the department. The authors would like to acknowledge the XPS facility at SRM University, Chennai.

References

1 S. Sharma and S. K. Ghoshal, *Renewable Sustainable Energy Rev.*, 2015, **43**, 1151–1158.
2 H. Wu, C. Feng, L. Zhang, J. Zhang and D. P. Wilkinson, *Electrochem. Energy Rev.*, 2021, **4**, 473–507.
3 J. Li, J. Hu, M. Zhang, W. Gou, S. Zhang, Z. Chen, Y. Qu and Y. Ma, *Nat. Commun.*, 2021, **12**, 3502.
4 X. Yan, B. Xu, X. Yang, J. Wei, B. Yang, L. Zhao and G. Yang, *Appl. Catal., B*, 2019, **256**, 117812.
5 H. Q. Fu, M. Zhou, P. F. Liu, P. Liu, H. Yin, K. Z. Sun, H. G. Yang, M. Al-Mamun, P. Hu, H.-F. Wang and H. Zhao, *J. Am. Chem. Soc.*, 2022, **144**, 6028–6039.
6 J. Li, H.-X. Liu, W. Gou, M. Zhang, Z. Xia, S. Zhang, C.-R. Chang, Y. Ma and Y. Qu, *Energy Environ. Sci.*, 2019, **12**, 2298–2304.
7 Z. Wang, Y.-R. Zheng, J. Montoya, D. Hochfilzer, A. Cao, J. Kibsgaard, I. Chorkendorff and J. K. Nørskov, *ACS Energy Lett.*, 2021, **6**, 2268–2274.
8 J. Chen, D. Yu, W. Liao, M. Zheng, L. Xiao, H. Zhu, M. Zhang, M. Du and J. Yao, *ACS Appl. Mater. Interfaces*, 2016, **8**, 18132–18139.
9 R. Rajalakshmi, A. Rebekah, C. Viswanathan and N. Ponpandian, *Chem. Eng. J.*, 2022, **428**, 132013.
10 Y. Lv, Z. Chen, Y. Liu, T. Wang and Z. Ming, *Nano-Struct. Nano-Objects*, 2018, **15**, 114–118.
11 H. Zheng and M. Mathe, *Int. J. Hydrogen Energy*, 2011, **36**, 1960–1964.
12 R. Rajalakshmi, C. Viswanathan and N. Ponpandian, *Sustainable Energy Fuels*, 2021, **5**, 5851–5865.
13 D. W. Su, J. Ran, Z. W. Zhuang, C. Chen, S. Z. Qiao, Y. D. Li and G. X. Wang, *Sci. Adv.*, 2023, **6**, eaaz8447.
14 A. C. Ghogia, S. Cayez, B. F. Machado, A. Nzihou, P. Serp, K. Soulantica and D. Pham Minh, *ChemCatChem*, 2020, **12**, 1117–1128.
15 L. Warczinski and C. Hättig, *J. Phys. Chem. C*, 2021, **125**, 9020–9031.
16 N. Yodsin, H. Sakagami, T. Udagawa, T. Ishimoto, S. Jungsuttiwong and M. Tachikawa, *Mol. Catal.*, 2021, **504**, 111486.
17 A. Ali and P. K. Shen, *Carbon Energy*, 2020, **2**, 99–121.
18 H. Yu, B. Zhang, C. Bulin, R. Li and R. Xing, *Sci. Rep.*, 2016, **6**, 36143.
19 Z. Song, G. Wang, Y. Chen, Q. Chang, Y. Lu and Z. Wen, *Chem. Eng. J.*, 2022, **435**, 134633.
20 H. C. Schniepp, J.-L. Li, M. J. McAllister, H. Sai, M. Herrera-Alonso, D. H. Adamson, R. K. Prud'homme, R. Car, D. A. Saville and I. A. Aksay, *J. Phys. Chem. B*, 2006, **110**, 8535–8539.
21 A. M. Dimiev and J. M. Tour, *ACS Nano*, 2014, **8**, 3060–3068.
22 J. Shi, Z. Cheng, L. Gao, Y. Zhang, J. Xu and H. Zhao, *Sens. Actuators, B*, 2016, **230**, 736–745.
23 Z. Q. Li, C. J. Lu, Z. P. Xia, Y. Zhou and Z. Luo, *Carbon*, 2007, **45**, 1686–1695.
24 S. Stankovich, D. A. Dikin, R. D. Piner, K. A. Kohlhaas, A. Kleinhammes, Y. Jia, Y. Wu, S. T. Nguyen and R. S. Ruoff, *Carbon*, 2007, **45**, 1558–1565.
25 S. P. Gupta, H. H. Nishad, S. D. Chakane, S. W. Gosavi, D. J. Late and P. S. Walke, *Nanoscale Adv.*, 2020, **2**, 4689–4701.
26 N. Minh Vuong, D. Kim and H. Kim, *Sci. Rep.*, 2015, **5**, 11040.
27 J. Kaur, K. Anand, K. Anand and R. C. Singh, *J. Mater. Sci.*, 2018, **53**, 12894–12907.
28 G. Jeevitha, R. Abhinayaa, D. Mangalaraj, N. Ponpandian, P. Meena, V. Mounasamy and S. Madanagurusamy, *Nanoscale Adv.*, 2019, **1**, 1799–1811.
29 J. V Rojas, M. Toro-Gonzalez, M. C. Molina-Higgins and C. E. Castano, *Mater. Sci. Eng. B*, 2016, **205**, 28–35.
30 D.-T. Phan and G.-S. Chung, *J. Phys. Chem. Solids*, 2013, **74**, 1509–1514.
31 V. Georgakilas, J. N. Tiwari, K. C. Kemp, J. A. Perman, A. B. Bourlinos, K. S. Kim and R. Zboril, *Chem. Rev.*, 2016, **116**, 5464–5519.
32 H. Liu and C. D. Vecitis, *J. Phys. Chem. C*, 2012, **116**, 374–383.

33 T. Tokunaga, T. Kawamoto, K. Tanaka, N. Nakamura, Y. Hayashi, K. Sasaki, K. Kuroda and T. Yamamoto, *Nanoscale Res. Lett.*, 2012, **7**, 85.
34 J. Baram, E. Shirman, N. Ben-Shitrit, A. Ustinov, H. Weissman, I. Pinkas, S. G. Wolf and B. Rybtchinski, *J. Am. Chem. Soc.*, 2008, **130**, 14966–14967.
35 V. Georgakilas, M. Otyepka, A. B. Bourlinos, V. Chandra, N. Kim, K. C. Kemp, P. Hobza, R. Zboril and K. S. Kim, *Chem. Rev.*, 2012, **112**, 6156–6214.
36 S. Lu, C. Blanco, S. Appleyard, C. Hammond and B. Rand, *J. Mater. Sci.*, 2002, **37**, 5283–5290.
37 H. Darmstadt, L. Sümmchen, U. Roland, C. Roy, S. Kaliaguine and A. Adnot, *Surf. Interface Anal.*, 1997, **25**, 245–253.
38 Y. H. Li, P. F. Liu, L. F. Pan, H. F. Wang, Z. Z. Yang, L. R. Zheng, P. Hu, H. J. Zhao, L. Gu and H. G. Yang, *Nat. Commun.*, 2015, **6**, 8064.
39 D. Yu, P. R. Ilango, S. Han, M. Ye, Y. Hu, L. Li and S. Peng, *Int. J. Hydrogen Energy*, 2019, **44**, 32054–32065.
40 T. Kou, M. Chen, F. Wu, T. J. Smart, S. Wang, Y. Wu, Y. Zhang, S. Li, S. Lall, Z. Zhang, Y.-S. Liu, J. Guo, G. Wang, Y. Ping and Y. Li, *Nat. Commun.*, 2020, **11**, 1–10.
41 H. Shen, H. Li, Z. Yang and C. Li, *Green Energy Environ.*, 2022, **7**, 1161–1198.
42 S. Zhang, Z. Xia, M. Zhang, Y. Zou, H. Shen, J. Li, X. Chen and Y. Qu, *Appl. Catal., B*, 2021, **297**, 120418.
43 M. Xiong, Z. Gao and Y. Qin, *ACS Catal.*, 2021, **11**, 3159–3172.
44 K. Wang, S. Wang, K. S. Hui, H. Gao, D. A. Dinh, C. Yuan, C. Zha, Z. Shao, Z. Tang and K. N. Hui, *Carbon Energy*, 2022, **4**, 856–866.
45 J. Dai, Y. Zhu, Y. Chen, X. Wen, M. Long, X. Wu, Z. Hu, D. Guan, X. Wang, C. Zhou, Q. Lin, Y. Sun, S.-C. Weng, H. Wang, W. Zhou and Z. Shao, *Nat. Commun.*, 2022, **13**, 1189.
46 J. Hu, E. M. Kim, M. J. Janik and K. Alexopoulos, *J. Phys. Chem. C*, 2022, **126**, 7482–7491.
47 S. Sun, X. Xiong, J. Han, X. Chang, N. Wang, M. Wang, Y. Lei, T. Liu and Y. Zhu, *ACS Appl. Nano Mater.*, 2019, **2**, 1313–1324.
48 P. Li, L. Liu, W. An, H. Wang, H. Guo, Y. Liang and W. Cui, *Appl. Catal., B*, 2020, **266**, 118618.
49 A. Manikandan, P. R. Ilango, C.-W. Chen, Y.-C. Wang, Y.-C. Shih, L. Lee, Z. M. Wang, H. Ko and Y.-L. Chueh, *J. Mater. Chem. A*, 2018, **6**, 15320–15329.
50 Y. Wang, B. Zhu, B. Cheng, W. Macyk, P. Kuang and J. Yu, *Appl. Catal., B*, 2022, **314**, 121503.
51 H. L. Nguyen, N. Hanikel, S. J. Lyle, C. Zhu, D. M. Proserpio and O. M. Yaghi, *J. Am. Chem. Soc.*, 2020, **142**, 2218–2221.
52 P. A. Shinde and S. C. Jun, *ChemSusChem*, 2020, **13**, 11–38.
53 R. Sharifian, R. M. Wagterveld, I. A. Digdaya, C. Xiang and D. A. Vermaas, *Energy Environ. Sci.*, 2021, **14**, 781–814.
54 Y. Chen, J. Yu, J. Jia, F. Liu, Y. Zhang, G. Xiong, R. Zhang, R. Yang, D. Sun, H. Liu and W. Zhou, *Appl. Catal., B*, 2020, **272**, 118956.
55 J. R. Varcoe, P. Atanassov, D. R. Dekel, A. M. Herring, M. A. Hickner, P. A. Kohl, A. R. Kucernak, W. E. Mustain, K. Nijmeijer, K. Scott, T. Xu and L. Zhuang, *Energy Environ. Sci.*, 2014, **7**, 3135–3191.
56 J. Li, in *PEM Fuel Cell Electrocatalysts and Catalyst Layers: Fundamentals and Applications*, ed. J. Zhang, Springer London, London, 2008, pp. 1041–1094.